Polarimetric Signatures in the Stratiform Region of a Mesoscale Convective System

D. S. ZRNIĆ

National Severe Storms Laboratory, Norman, Oklahoma

N. BALAKRISHNAN

Department of Aerospace Engineering, Indian Institute of Science, Bangalore, India

C. L. ZIEGLER

National Severe Storms Laboratory, Norman, Oklahoma

V. N. BRINGI

Department of Electrical Engineering, Colorado State University, Fort Collins, Colorado

K. AYDIN

Communications and Space Sciences Laboratory, Pennsylvania State University, University Park, Pennsylvania

T. MATEJKA

National Severe Storms Laboratory, Norman, Oklahoma

(Manuscript received 10 November 1991, in final form 5 February 1992)

ABSTRACT

Four polarimetric measurands were collected in the stratiform region of a mesoscale convective system. The four are the reflectivity factor, the differential reflectivity, the correlation coefficient between orthogonal copolar echoes, and the differential propagation constant. Most striking is a signature of large aggregates (about 10 mm in size) seen in the differential phase through the melting layer. Another significant feature is an abrupt notch in the correlation coefficient that occurs towards the bottom of the bright band. Aircraft observations and a one-dimensional cloud model are used to explain some polarimetric measurements and to infer the presence of aggregates, graupel, and supercooled cloud water in the stratiform region. These unique observations and model data provide inferences concerning the presence of graupel and the growth of large aggregates in the melting layer.

1. Introduction

A long-standing problem in meteorology is that of distinguishing, by remote probing radars, various types of precipitation. Several single and multiparameter radar techniques have been directed toward this problem (for instance, see special issue of *Radio Science,* **19,** No. 1, January–February 1984).

Polarization radars provide measurements of several independent echo characteristics. This additional information can be used, in principle, to estimate parameters such as the mean value and the breadth of the distribution of sizes or shapes, the spatial orientation of particles filling the radar resolution volume, their thermodynamic phase, as well as the bulk properties of the intervening medium. But even the most advanced radars obtain fewer independent measurands than necessary to estimate all parameters of precipitation. Hence, to interpret the radar observations, scientists rely on additional experimental–theoretical evidence that relates the size, shape, and spatial orientations of hydrometeors. Even with such simplifying assumptions, the interpretation of backscattered signals from a single resolution volume is difficult. This is because several precipitation models yield the same backscatter signatures; that is, the inverse problem is not unique. Therefore, one needs to capitalize on the ability of the radar to scan a volume; from spatial profiles of polarization variables it is possible sometimes to infer precipitation habitats and thermodynamic phase.

In this paper, the stratiform region of a mesoscale convective cloud system that formed on 3 June 1989 is examined with both in situ and remote-sensing instruments. Because the stratiform region is horizontally extensive compared to its depth, it is well suited for generalizing interpretations from spatial measurements in one and two dimensions. This case serves as a specimen for testing the utility of polarimetric measurands to diagnose the type of hydrometeors present and also

Corresponding author address: D. S. Zrnić, Chief, Doppler Radar and Remote Sensing Research, National Severe Storms Laboratory, 1313 Halley Circle, Norman, OK 73069.

provides an opportunity to learn about microphysical processes in this exceptional mesoscale system. A one-dimensional cloud model with parameterized microphysics is used to independently diagnose the vertical distribution of water substance for the purpose of validating hypotheses based on the polarimetric and in situ measurements.

2. Observations

On the evening of 3 June 1989, a mesoscale convective system (MCS) passed over north central Oklahoma during the Cooperative Oklahoma P-3 Studies (COPS-89) project. Polarimetric data were collected in this system to address an objective of COPS-89, namely, to investigate how polarimetric data may be used to infer the habits and sizes of precipitation particles. Figure 1a depicts the radar reflectivity at 2130 (all times are CST). An extensive stratiform region covered most of Oklahoma, while convective radar echo cores were located along the Red River and in west Texas. Several measurements with different instruments were made through the stratiform region of the MCS. A dual-Doppler analysis was performed within the region denoted by a dashed box using data collected by the Norman and Cimarron radars (wavelength 10 cm) at about 2134 (Matejka and Ziegler 1990). Locations where data were collected are shown in Fig. 1b together with the reflectivity factor contours of the MCS.

Polarimetric radar data consisting of complex weather signals at alternate vertical and horizontal polarizations were collected at 2109 in a range–height mode. The National Oceanic and Atmospheric Administration (NOAA) P-3 aircraft, which was equipped with a two-dimensional cloud probe (Knollenberg 1970), executed a spiraling descent in the stratiform region starting at 2157 (7 km above ground level) and ending at 2229 (2.7 km AGL). A radiosonde was launched through the system from the National Severe Storms Laboratory (NSSL) mobile-CLASS (M-CLASS) platform at 2243 (Fig. 2a). This sounding provides profiles of pressure, temperature, water vapor, and horizontal wind from the stratiform region. (The loran signal was lost for a portion of the flight, hence no middle level winds were obtained.) Data from the M-CLASS and the aircraft descent sounding were used to determine the temperature profile for interpretation of radar measurements. From those soundings, the melting level was determined to be at 3.4 km. The weather signals were processed to produce the reflectivity factor Z, the differential reflectivity Z_{DR}, the correlation coefficient between copolar echoes $|\rho_{hv}(0)|$, and the two-way differential propagation constant K_{DP}, which is the range derivative of the differential phase ϕ_{DP} (Balakrishnan and Zrnić 1990a,b). Positive differential reflectivities are produced by hydrometeors whose longer dimensions are aligned with the horizontal axis (this is true at a 10-cm wavelength for scatterers

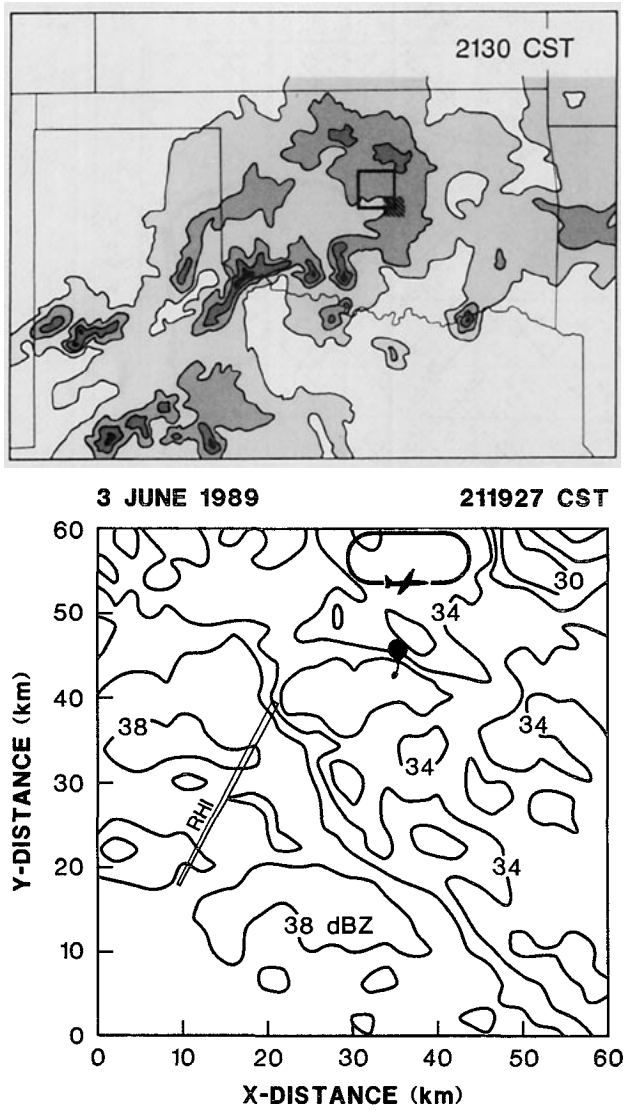

FIG. 1. (a) The reflectivity field of the mesoscale convective system on 4 June 1989. The composite is from several radars and for 2130 CST. Countours are in steps of 10 dBZ starting at 20 dBZ, and the Cimarron radar is located at the lower left corner of the square. The dashed box locates the dual-Doppler analysis region. (b) Detail of the field corresponding to the 60-km × 60-km square area in (a) that was obtained with the Cimarron radar. The elevation angle is 1.1°, and the location of data-gathering instruments is indicated.

with diameter less than about 40 mm). Similar condition produces positive K_{DP}; yet the dependencies of K_{DP} and Z_{DR} on size and oblateness of hydrometeors are different. Also, as shown in this paper, hydrometeors having a narrow size range (centimeter size) produce distinct signatures in the ϕ_{DP} data. The correlation coefficient has values close to 1 in regions populated by single types of relatively smooth, small hydrometeors; scatterers that have various sizes, axial ratios, and a distribution of canting angles (i.e., they wobble) cause a decrease of the correlation coefficient (Balakrishnan and Zrnić 1990b).

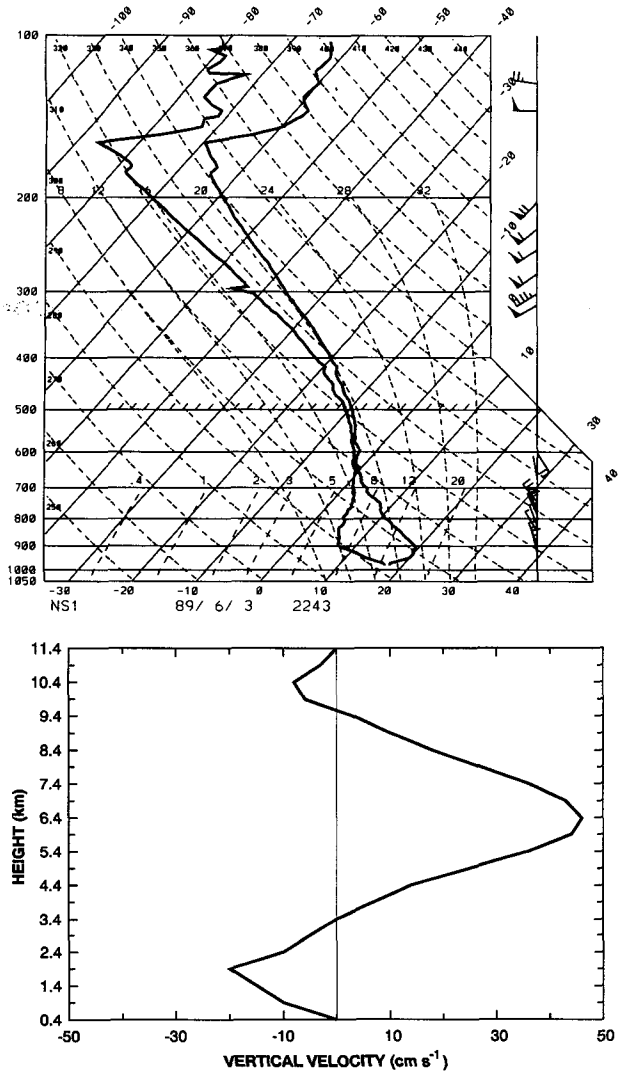

FIG. 2. (a) Composite sounding in the stratiform region from the M-CLASS release at 2230 CST 3 June 1989. (b) Vertical velocity profile obtained from the dual-Doppler analysis and used in the model.

Aircraft measurements started at 2159 (50 min after the polarimetric measurements). Shadowgraphs from the airborne cloud probe were available (but the two-dimensional particle probe on the aircraft was not functional). From these it is not possible to precisely determine sizes and concentrations of large hydrometeors because the cross section of the sampling volume (sweeping area 1.67 mm × 6 mm and length 140 m $s^{-1} \times T$, where the time T is tens of seconds) is very small; nevertheless, quantitative information about particles smaller than 1.6 mm and qualitative impressions about the types and relative sizes and concentrations of larger species can be deduced. Thus, some general inferences are possible through comparisons between aircraft, radar, and model data because the stratiform part of the system was in steady state and was fairly homogeneous.

3. Numerical cloud model

A one-dimensional kinematic numerical cloud model was used to estimate the vertical profiles of cloud and precipitation in the stratiform region of the 3–4 June MCS. The column representing the model domain may be conceptualized as moving in a quasi-Lagrangian reference frame with the mean motion of the mesoscale updraft and the coincident reflectivity core of the stratiform region. Although horizontal advection with the mean wind should be zero in the aforementioned reference frame, the effects of differential horizontal advection due to vertical shear of the horizontal wind are not explicitly represented. Since differential horizontal advection of ice from the convective region at high levels probably seeded the mesoscale updraft, the assumption of a fixed ice content at the top of the model domain was employed to implicitly simulate this "seeder–feeder" mechanism (Rutledge and Hobbs 1983).

We employed a version of the model developed by Ziegler et al. (1986), which was modified to include snow-particle aggregation. The new snow parameterization is documented in the Appendix; other microphysical processes are modeled as in Ziegler (1985). Independent continuity equations describe the profiles of potential temperature, the mixing ratio of water vapor and cloud ice, and the total concentrations and mixing ratios of cloud droplets, rain drops, graupel, and snow particles. Important microphysical processes in the model include ice nucleation and deposition growth, riming and aggregation of snow particles, melting of ice particles and raindrop evaporation and self-collection. Graupel is formed from two sources: 1) autoconversion of cloud liquid to drizzle-sized rain droplets that subsequently freeze and 2) aggregated snow particles that collect and freeze supercooled cloud droplets during their descent to the melting level. Mass-weighted mean diameters of both particle types must exceed 3 mm to qualify. The model domain is composed of 111 grid points spaced at 100-m intervals vertically from 0.4 to 11.4 km.

The temperature and water vapor mixing ratio profiles were initialized by interpolating to the model grid the sounding obtained in the stratiform region (Fig. 2a). An upper boundary condition on snow content was imposed in the model calculations to approximate the previously noted seeder–feeder effect. Because data on ice concentrations at the tops of stratiform regions were not available (in this or other cases), two model runs were performed with different values of snow concentrations at the top of the model domain (11.4 km). The observed reflectivity (about 10 dBZ) was combined with an assumed snow-particle concentration via the known analytic expressions for reflectivity and size distribution to compute the corresponding snow mixing ratio. Values of snow concentration of 1, 10, and 100 L^{-1} were considered, from which snow

mixing ratio (mean diameter) values of about 0.1 g kg^{-1} (0.5 mm), 0.3 g kg^{-1} (0.4 mm), and 1.1 g kg^{-1} (0.3 mm) were computed, respectively. Heymsfield (1986) observed ice contents of up to about 1 g kg^{-1} at 9.3 km in the forward overhang (anvil) of a convective storm, whereas Willis and Heymsfield (1989) observed ice contents of about 0.5 g kg^{-1} at 5.5 km in the stratiform precipitation region of an MCS. The ice particles comprising their samples had grown by diffusion during fall through the cloud toward the sampling level and therefore had originated higher in the cloud where ice content was probably considerably lower than 1 g kg^{-1}. We rejected high ice-particle concentrations [$O(100\ L^{-1})$] as upper boundary values for our model calculations because the ice contents implied near the top of the stratiform region were too large. But the 0.1–0.3 g kg^{-1} values of ice content (corresponding to the 1–10 L^{-1} range of ice concentration) were consistent with the aforementioned measurements. Hence, the values of 1 and 10 L^{-1}, respectively, were tried as the snow concentration at the upper boundary in two model runs. These boundary values of concentration and mixing ratio of snow were held constant during the model integration. The initial hydrometeor content was assumed to be zero at all model levels below 11.3 km and was free to change during integration.

The model integration procedure was simplified since the kinematic analyses covered only a small volume and only a fraction of the lifetime of the MCS. In contrast to integrating with a time-varying vertical velocity profile as in Ziegler et al. (1986), the model was instead integrated in two stages utilizing a constant updraft profile. The first stage was to integrate for 3 h with the mesoscale updraft set to zero, at which time the snow and meltwater rain profiles were in steady state and other hydrometeor fields had zero values. These precipitation profiles, presumed to approximate conditions adjacent to the mesoscale updraft region, were used to initialize the second stage in which an observed mesoscale updraft profile was input to the model for computing vertical advection and mixing terms. By initializing the precipitation profiles in this manner, the presumed seeding effect of the updraft was crudely approximated from horizontal advection of ice into the updraft region. Proceeding from the steady-state initial profiles and the observed updraft profile, the model was integrated for an additional 120 min to estimate the impact of the mesoscale updraft. The vertical velocity profile was computed by horizontally averaging vertical velocity values derived from a dual-Doppler analysis performed in the dashed box in Fig. 1 (Matejka and Ziegler 1990). The resulting vertical velocity profile (Fig. 2b) contains values ranging from −20 cm s^{-1} at 1.9 km to 46 cm s^{-1} at 6.4 km. The purpose of this second stage of integration was to determine if the model could generate and maintain a deep supercooled cloud layer and graupel in the mesoscale updraft (as observed), and if so to gain insight into the mechanisms involved. A more quantitative interpretation might be possible with a version of the model that includes two or more space dimensions and evolutions (e.g., Ziegler et al. 1991), although that was not attempted here.

4. Results

a. Overview and interpretation of model output

After 60 min of integration with the mesoscale updraft activated in the run assuming a snow concentration of 10 L^{-1} at the top of the domain, the model predicted formation of a liquid cloud layer topped by a cloud ice layer along with a mixture of aggregated, rimed snow particles and graupel. Between 60 and 120 min of integration, the liquid cloud was converted to cloud ice. This conversion of cloud liquid to cloud ice was due to the lower vapor pressure over ice than over water, which accelerated diffusion growth of numerous small ice particles at the expense of cloud droplets. (This diffusional growth of ice at the expense of liquid droplets is known as the Bergeron process.) Cloud droplets evaporated because the mesoscale updraft was not of sufficient intensity to maintain the local vapor supply against the rate of depletion of vapor by diffusion. By 120 min, only a shallow layer of liquid cloud remained near the melting level. This shallow supercooled cloud layer had insufficient content to allow ice particles to grow by riming, hence graupel was virtually absent by 120 min.

Elements of the above scenario are similar to the "type-2" (seeder–feeder cloud with mesoscale updraft) discussed by Rutledge and Hobbs (1983). Whereas Rutledge and Hobbs diagnosed a liquid cloud layer of nearly constant peak water content in their modeling study, the present model output suggests that the supercooled cloud layer in the middle levels of the 3 June stratiform region should be of a transitory nature. This is mainly due to the presence of abundant ice particles growing by deposition in the mesoscale updraft in middle levels of the stratiform region of the 3 June MCS. The period of time over which the supercooled cloud could persist is likely to be quite sensitive to the cloud ice nucleation rates assumed by the model, as well as the snow-particle concentration assumed at the top of the model domain; low (high) ice concentrations lead to underseeding (overseeding) and persistence (decay) of the supercooled cloud. Unfortunately, ice particles smaller than 100 μm cannot be identified from the cloud-probe data and hence cannot validate the modeled ice nucleation rates. Nevertheless, a second model run was performed assuming a snow-particle concentration of 1 L^{-1} at the top of the domain to determine the impact of snow-particle concentration on hydrometeor profiles in the mesoscale updraft region. The resulting hydrometeor profiles (not shown) are

qualitatively similar to the profiles obtained from the first model run. Results suggest, however, that lowering the snow concentration above the mesoscale updraft reduces the maximum snow-particle concentration and increases both the supercooled cloud content and the period of time over which the supercooled cloud persists. For example, the profiles at 120 min in the run assuming an upper boundary value of snow concentration of 1 L^{-1} are similar to the profiles at 60 min in the run assuming an upper boundary value of snow concentration of 10 L^{-1}.

b. Comparison of model output to microphysical measurements

Both model output and cloud-probe data analysis confirm the presence of supercooled liquid cloud and graupel, as well as snow and rain (Fig. 3). We select the model output 1 h after the inclusion of the updraft. The vertical profiles of the measured and modeled mean sizes are in quantitative agreement except for snow sizes in the melting layer (Fig. 3a); there the measurements show a further increase with decreasing height not present in the model. This is probably because the model lacks detailed resolution of particle size distribution and does not include melting-aggregation rate in the melting layer. The model calculations demonstrate that the ice-supersaturated conditions between the melting level and the storm top (maintained by the mesoscale updraft) provide for efficient depositional growth of the snow particles.

Shadowgraphs indicate that the numbers of graupel and aggregate particles were about the same in the height interval 3.4–6.4 km (Fig. 3b). Modeled concentration are 25%–33% of observed graupel concentrations. The modeled snow-particle concentration is comparable to the observed aggregate concentrations at the melting level, while modeled snow-particle concentrations are one order of magnitude higher than observed values above 5 km; note that the model value is a total concentration that includes numerous small aggregated particles. The model produces a supercooled

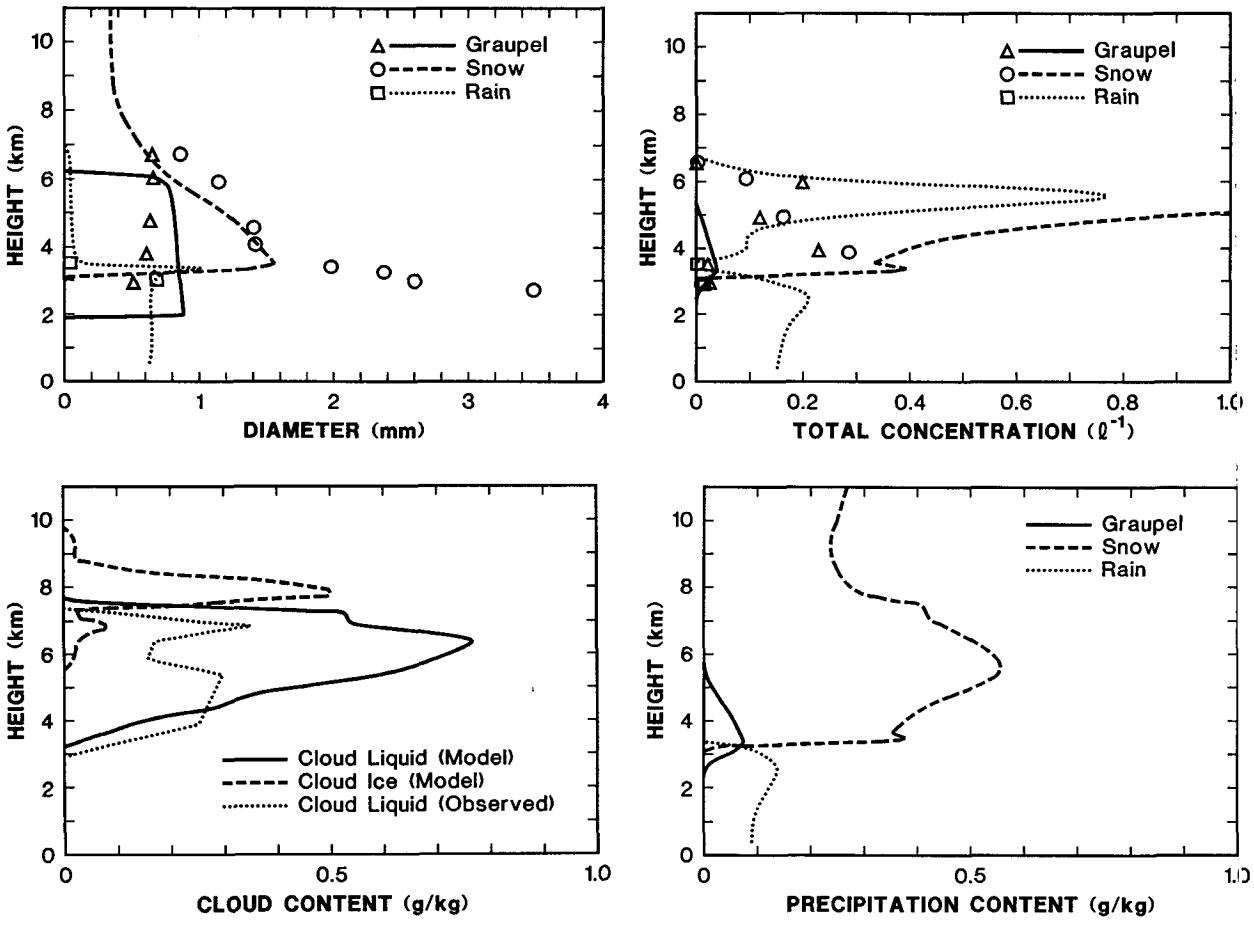

FIG. 3. Height profiles of (a) mean diameters of hydrometeors from a one-dimensional cloud model (curves) and from observations (symbols) by a two-dimensional cloud probe on board the P-3 aircraft, (b) observed and modeled concentrations of the dominant hydrometeors, (c) cloud ice and liquid water content from the model and observed (with a JW hot-wire probe on board the P-3 aircraft) liquid water content, and (d) modeled precipitation content of dominant hydrometeors.

liquid cloud from about 3.4 to 8 km (Fig. 3c), and this agrees very well with in situ measurements on the P-3 aircraft, except the peak observed liquid water content is smaller than the peak modeled liquid water content by a factor of two. Nevertheless, the model calculations support the notion that the measured liquid water content (roughly 0.4 g kg^{-1}) in the stratiform region is significant and sufficient to promote graupel growth. A twofold increase in snow mixing ratio in middle levels (Fig. 3d) is caused by vapor diffusion growth of snow particles, while just under 0.1 g kg^{-1} of graupel is generated above the melting level. Rain content increases from melting of snow and graupel, reaching a maximum near 2.5 km as graupel vanishes.

c. *Polarimetric measurements*

Vertical profiles of polarimetric measurands were obtained in the range–height indicator (RHI) scan mode about 50 min (2109) before the aircraft began a spiral descent and about 100 min before the sonde launch. The reflectivity factor, the differential reflectivity, the correlation coefficient, and the differential phase constant are shown in Fig. 4; these are from the region indicated in Fig. 1b. Height profiles are plotted in Fig. 5, where Z and Z_{DR} are average values within 100-m increments in height, whereas K_{DP} and $|\rho_{hv}(0)|$ are not averaged.

Reflectivity profiles from the areal average, the model, and the nadir direction of the aircraft radar (3-cm wavelength) are also included in Fig. 5a. The remarkable similarity between all these reflectivity profiles suggests that steady-state conditions existed in the stratiform region. The reflectivity (measured from RHIs at close range) increases first gradually with the decrease (Fig. 5a) in height until about 4 km and then rises sharply to form a brightband peak at 3.2 km; this is 200 m below the melting level (determined by balloon and aircraft measurements). The areal-averaged reflectivity profile has a broader brightband peak because data are from farther ranges, they have been interpolated to a grid with 500-m spacings, and the average at each level is over a 30-km × 30-km area in the center of the stratiform region. The reflectivity profile obtained from the model resembles the averaged from radar analysis, suggesting that the model reliably estimates the areally averaged profiles of concentration, average particle size, and phase of precipitation.

Differential reflectivity is slightly positive (0.1 dB) at a height of 8 km (Figs. 4b and 5b), possibly because ice (snow) particles are horizontally oriented there. It decreases at 6 km to form a well-defined band of slightly negative (−0.05 dB) Z_{DR} values situated between 3.5 and 6 km. This is the region where the reflectivity is larger than 15 dBZ, and it is also there that the model (Fig. 3a) predicts modest amounts of graupel, about 0.8 mm in diameter and total concentration of 0.03 L^{-1} (Fig. 3b). The mean diameter, computed from the cloud-particle probe data, is 0.6 mm, and the median volume diameter D_0 is 0.8 mm. Graupel may be responsible for the negative differential reflectivity seen by the radar. Computations by Aydin and Seliga (1984) indicate that small graupel ($D_0 < 1$ mm) would produce slightly negative Z_{DR} but larger sizes would have positive values. A legitimate concern is the possibility that the small values of Z_{DR} may have been caused by a bias. Checks by pointing the beam vertically have been made; because there is no preferred particle orientation perpendicular to the beam axis, an average Z_{DR} value of 0 dB is expected. This indeed was the case and the standard deviation about this mean was 0.4 dB. Furthermore, the relative echo strengths in the vicinity of the beam suggest that sidelobe contamination was not important. Thus, the observed decrease at 6 km is probably not an artifact.

A noteworthy feature in the correlation is the high mean value above 4 km. It is speculated that this is because snow particles and graupel are small and their wobbling is not substantial. The model and observations (Figs. 3a–c) indicate that a mixture of cloud ice crystals and some larger snow particles are present above 6 km. Cloud ice particles in the model are about 10 μm in diameter; with peak mixing ratio of 0.5 g kg^{-1} the computed concentration for the gamma distribution (see the Appendix) is up to about 600 cm^{-3} at 8 km. The increased standard deviation in $|\rho_{hv}(0)|$ at these heights is caused by noise (signal-to-noise ratios near unity); the estimates are corrected for the noise bias and that is also the reason that some values are larger than 1.

The differential propagation constant K_{DP} (Fig. 4d) has not been smoothed, and therefore the field is not very coherent. Generally the values above the freezing level are about zero, but below the freezing level there appears to be significant contribution from differential phase shift upon scattering. This becomes more evident in the height profile of these data (Fig. 5d) that were obtained after filtering the differential phase shift ϕ_{DP} with a running median filter; each data value was replaced with a median of nine consecutive data, thus, for samples spaced 450 m in range, the smoothing distance was 4 km. Furthermore, $d\phi_{DP}/dr$ was obtained from a least-squares fit of a linear function over the same 4-km distance. On either side of the bright band are positive excursions of K_{DP}.

5. Interpretation of polarimetric measurements in the melting layer

The abrupt drop in the correlation coefficient from 1 to about 0.86 over a 600-m depth, between 2.5 and 3.1 km (Fig. 5c), is very striking. The peak of differential reflectivity associated with the bright band is at the lowest height of 2.5 km, and barely 300 m above it is the dip in the correlation coefficient similar to the observation by Illingworth and Caylor (1989). An em-

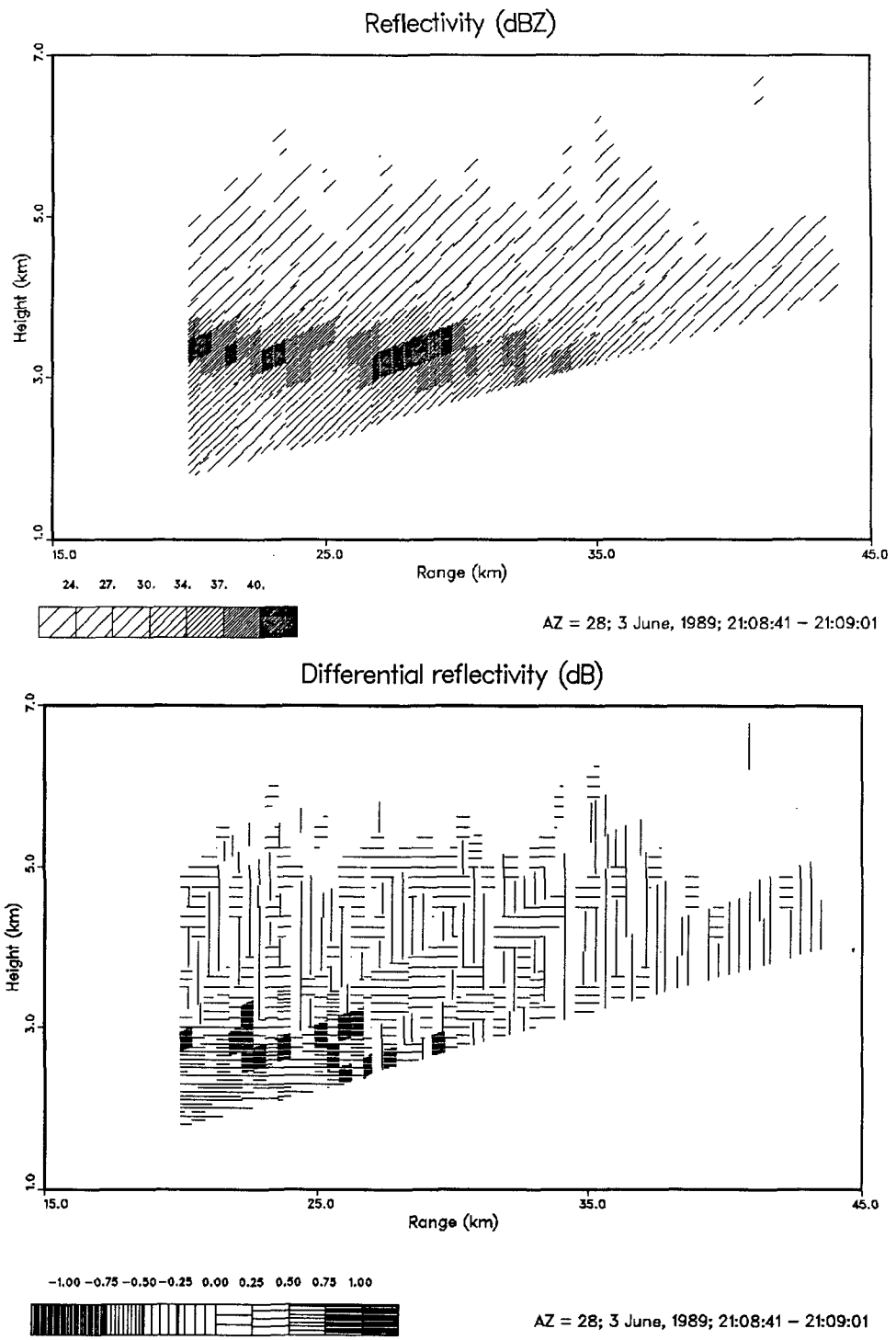

FIG. 4. Range-height cross sections of (a) reflectivity factor Z, (b) differential reflectivity Z_{DR}, (c) correlation coefficients $|\rho_{hv}(0)|$, and (d) differential propagation constant K_{DP}.

pirical explanation for the position of these peaks is as follows. Wetting on the outside of snow aggregates (or other ice particles) and then further coalescence is first detected as an increase in reflectivity. But as rain drops form, they have smaller cross sections than the wet ice hydrometeors from which they originated and have increased fall speed; hence, reduced concentration due to flux divergence of particles and their smaller cross

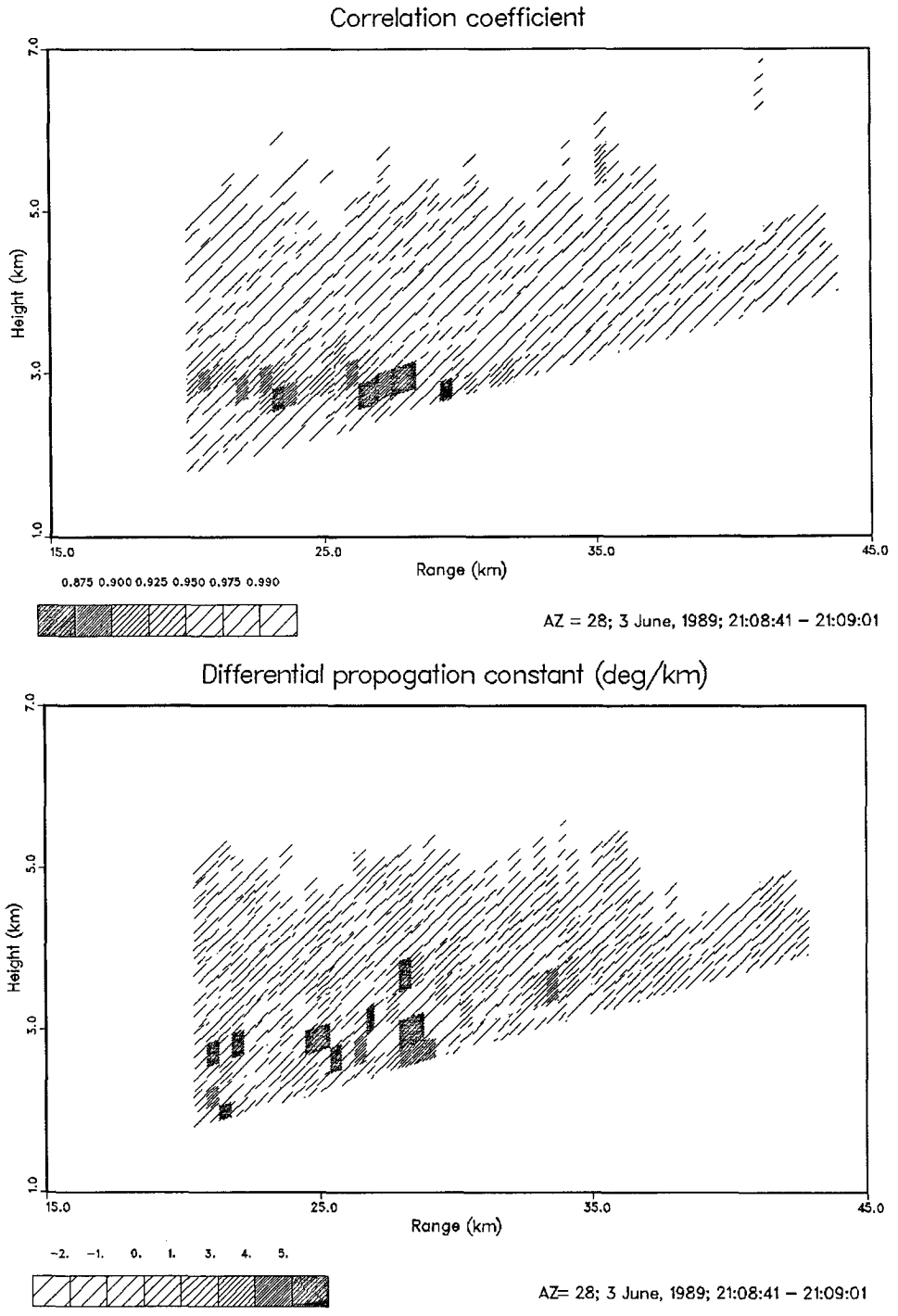

FIG. 4. (*Continued*)

section decreases the reflectivity. As melting progresses, the variety of shapes and sizes increases with the addition of raindrops; furthermore, some aggregates continue to grow by combining with other aggregates. These factors could have contributed to a rapid drop in $|\rho_{hv}(0)|$ at about 2.8 km (Jameson 1989), but it will be demonstrated later that the dominant contribution to the decrease is from the variations of the differential phase shift upon scattering. It is likely that large but not completely wet aggregates are present at this height; note that large aggregates are found at 4°C (height of 2.75 km in Fig. 3a). This is further corrob-

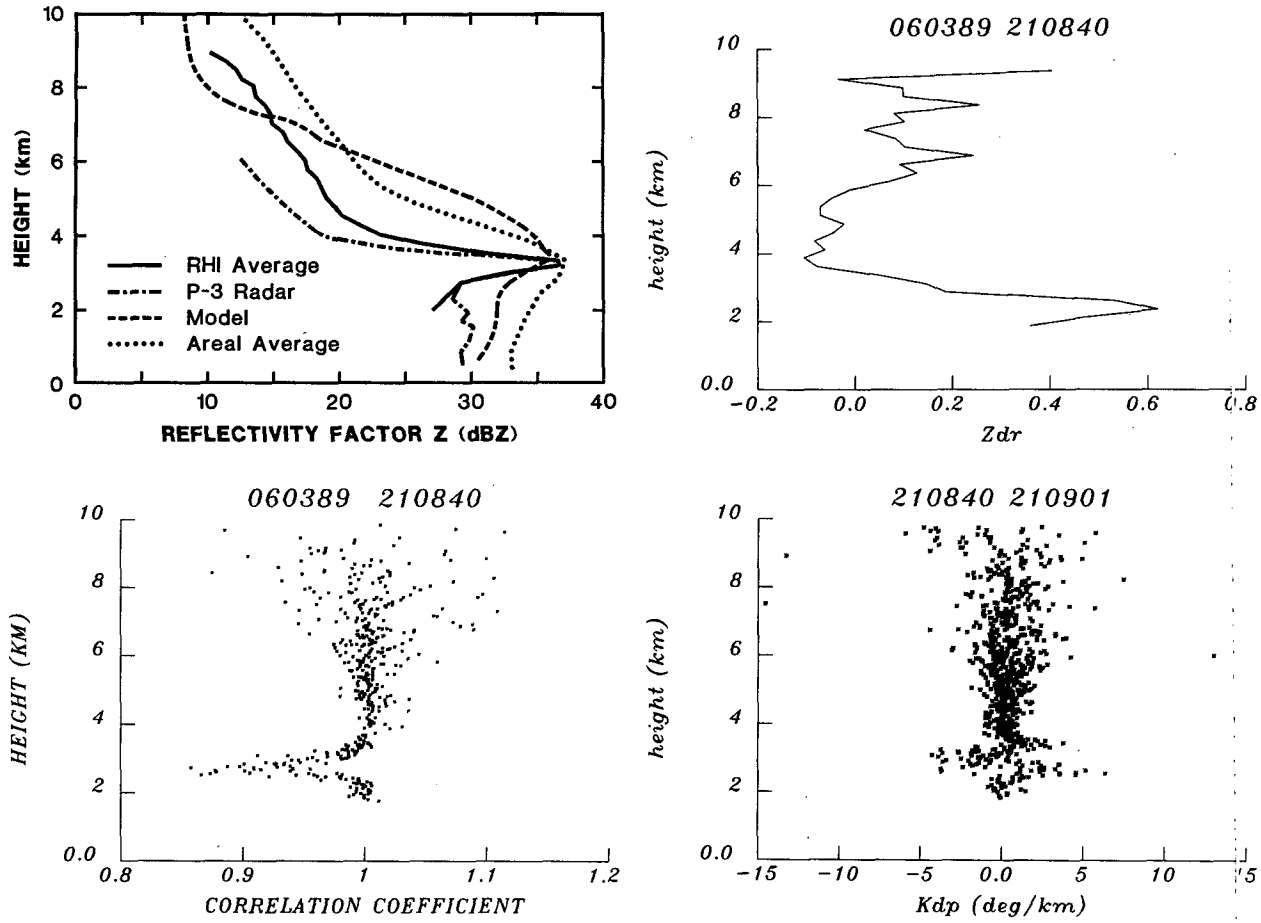

FIG. 5. Height profiles of (a) average reflectivity, (b) average differential reflectivity, (c) correlation coefficient, and (d) differential propagation constant for the data in Fig. 3.

orated by the peak in the differential reflectivity (Fig. 5b; Table 1), which is offset 300 m downward from the dip in $|\rho_{hv}(0)|$. The fact that the abrupt drop in the correlation coefficient occurs through a layer less than 600 m deep prompted detailed examination of the data, which suggests that the transition zone (i.e., the location of the minimum in $|\rho_{hv}(0)|$) is smaller than 200 m and beam smoothing has spread the signature. Although precipitation data at the height of maximum Z_{DR} (2.5 km; Table 1) is not given, extrapolation from Fig. 3a leads us to deduce that the peak is caused by water-soaked aggregates. Polarimetric measurands are little affected by dry aggregates because these have a low dielectric constant and are small. Wet aggregates tend to fall with a minor axis vertical, which is the orientation with minimum energy (i.e., slowest fall speed). Just before collapsing into drops, the aggregates have reached their biggest size, and although their relative number is small, their contribution to differential reflectivity is largest here. The raindrops are too small (mean sizes up to 0.6 mm) to affect differential reflectivity. Note that the distance of 700 m between the maximum of Z and the maximum of Z_{DR} (Table 1) is 3.5 times larger than a value found in a melting layer in Colorado (Moninger et al. 1984). This suggests that the aggregates must have considerable size to survive a long fall. Although cloud-probe data contained sizes larger than 3 mm (Fig. 3a) and the dimension (along the aircraft flight path) of some aggregates was from 8 to 12 mm, these data cannot be used to estimate the actual size; further speculation about the size is possible from the differential phase measurements and will be discussed shortly.

TABLE 1. Heights (km) in the melting layer at which extreme values occurred.

	Z	Z_{DR}	K_{DP}	$\lvert\rho_{hv}(0)\rvert$
Positive peak	3.2		3.4	
Negative peak			3	2.8
Positive peak		2.5	2.5	

Large positive excursions of K_{DP} have been noted below (at 2.5 km; Table 1) and at the melting level

(3.4 km). To explain this profile, we use the data along a radial through the melting layer, which corresponds to the increase in reflectivity extending in range from 27 to 37.5 km. The differential phase (ϕ_{DP} in Fig. 6) exhibits an abrupt increase of 4° at 29 km, which is precisely at the bottom of the melting layer (i.e., height above ground of 2.5 km where melting of all hydrometeors has just been completed). In general, this differential phase is comprised of a cumulative propagation phase shift and a phase shift upon backscattering δ; the latter becomes significant if hydrometeors are large such that the scattering is in the resonant regime. We believe that δ is responsible for the sharp rise in Fig. 6. Similarly, the sharp drop starting at 33 km might also be due to differential phase shift upon scattering.

Consideration of scattering model results and physical arguments further substantiate this speculation concerning the sharp drop in ϕ_{DP}. Aggregates coated with substantial amounts of water have polarimetric properties similar to water-filled aggregates of the same size; this is by analogy to a spherical ice mass that appears to the radar as a liquid hydrometeor if water coating thickness is 10% of the radius (Battan 1973). Therefore, the hydrometeors are assumed to be composed of liquid water with the caveat that sizes of wet aggregates are close to their image size but might be considerably larger than the equivalent melted diameters. The differential phase shift upon scattering for a heavily water-coated oblate spheroid (axis ratio 0.8) has a transition in sign at a diameter of about 10 mm (Fig. 7). Other axis ratios lead to similar results that are obtained using Waterman's formulation (1969); for example, an axis ratio of 0.6 produces a transition at the same equivolume diameter but the positive and negative excursions are twice as large. Similar calculations were performed for a spongy mixture of water and ice. As the percentage of ice increases, the phase transition shifts towards larger diameters and occurs at 2.7 cm for pure ice. Therefore, and because of melting at 4°C, we conclude that aggregates slightly larger than 1 cm could have produced the positive increase of differential phase. This is also in accord with the increase of Z_{DR} previously noted in Fig. 5b. It appears that at higher altitudes in the melting layer (3–3.3 km, range 33–36 km in Fig. 6), there is a general decrease in the sizes of wet aggregates that contributes significantly to δ; note that the scattering model produces negative δ for sizes 7–10 mm in diameter (Fig. 7). Thus, the negative excursion of the differential phase (at 3.3 km in height, 36 km in slant range) may have been produced by particles mainly in the size range 7–10 mm. Note that in the absence of large hydrometeors, the differential phase would have followed the dotted line in Fig. 6, and the K_{DP} ($d\phi_{DP}/dr$) would have been small but positive.

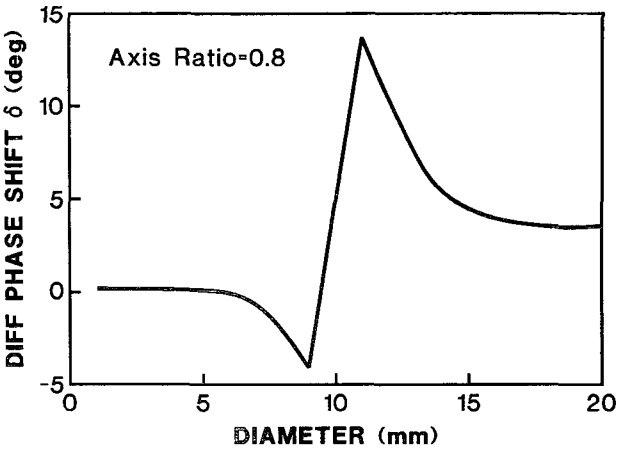

FIG. 7. Differential phase shift upon backscatter of a water spheroid. Axis ratio is 0.8 and the orientation is with the minor axis vertical.

A schematic in Fig. 8 summarizes the observed trends in ϕ_{DP} and K_{DP}. Contributions from propagation and differential phase shift upon scattering δ are indicated, the radar resolution volumes V_6 have spheroidal shapes that stem from a Gaussian antenna pattern and an almost Gaussian range weighting function (Doviak and Zrnić 1984). The differential propagation constant K_{DP} and differential phase ϕ_{DP} approximately represent the actual measurements.

To demonstrate that the described speculation is feasible, self-consistency among the polarimetric measurands was checked. The following simple computation was used for the bottom of the melting layer because there the effect is most pronounced. Assumptions are that the reflectivity factor is comprised of a part Z_r, which is produced by small rain drops, and a part (Z_h or Z_v), which is polarization-dependent due to aggregates. Furthermore, the aggregates are assumed to be wet and represented with one average size (about 12 mm) and axis ratio of about 0.8. Measured quantities used in this consistency check are the reflectivity factor Z_r of 501 mm^6 m^{-3} (27 dBZ), the differential

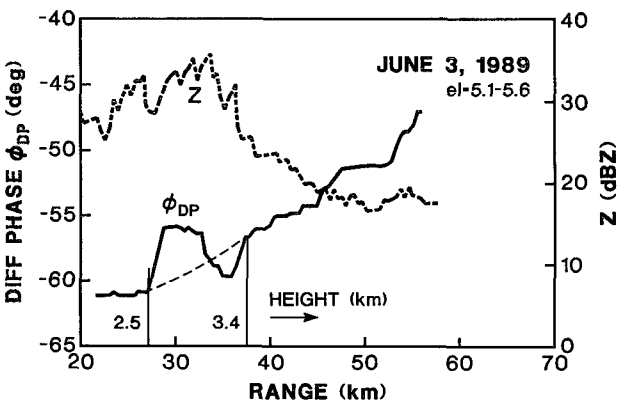

FIG. 6. Profiles along a radial through the melting layer at an elevation of 5.2°, (a) reflectivity factor and (b) differential phase.

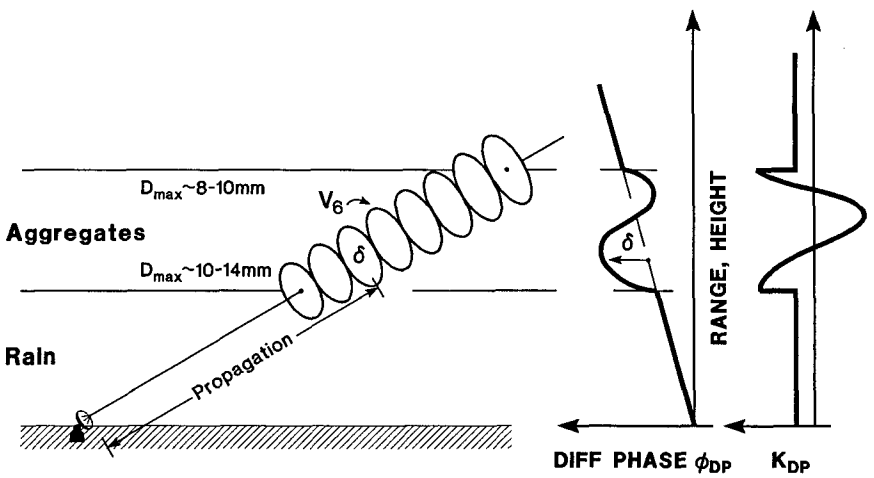

FIG. 8. Conceptual representation of the change in differential phase and differential phase constant along a radial through the melting layer.

reflectivity of 0.6 dB (Fig. 4b), and the differential phase upon scattering of $\delta_m = 4°$ (Fig. 6). It can be shown that the relationship between δ_m and the theoretical (for a wet oblate spheroid) $\delta = 10°$ is

$$\arg[Z_r + (Z_h Z_v)^{1/2}\exp(j\delta)] = \delta_m.$$

Now, for a 0.8 axis ratio, $Z_h = 1.67Z_v$. From the above equation we find $Z_v = 257$ mm^6 m^{-3} and $Z_{DR} = 10\log[(Z_r + Z_h)/(Z_r + Z_v)] = 0.8$ dB; this is quite close to the measured 0.6 dB (Fig. 5b).

Thus far, the only other observations of the correlation coefficient in the melting layer were made by Illingworth and Caylor (1989), who noted a drop similar to ours. Balakrishnan and Zrnić (1990b) suggest that a mixture of hydrometeors, the distributions of sizes and shapes, and the differential phase shift upon scattering could cause the reduction of $|\rho_{hv}(0)|$. It appears in the present dataset that the variations of δ (not seen in ϕ_{DP} because of the smoothing by the median filter) are the most significant contributors to the reduction in $|\rho_{hv}(0)|$ (Figs. 4c, 5c). Note that the $|\rho_{hv}(0)|$ minimum is within the height interval where K_{DP} is negative (200 m below the center; Table 1), which is precisely the region were the transition in size and in δ occurs. Further measurements of δ at C band are provided by Meischner et al. (1991), who attribute large values to melting of small hail.

6. Discussion

a. *Supercooled cloud water and graupel in the stratiform region*

In situ observations in the stratiform region of the 3 June 1989 MCS reveal presence of graupel that is reproduced by a one-dimensional cloud model. While in other cases the origin of graupel can be traced to the convective region from which it is transported by horizontal advection, the active convection in the 3 June system was over 200 km southwest of the region in which our data were collected (Fig. 1a). Therefore, it is unlikely that graupel came from the leading squall line, however, graupel could have been generated locally. A mesoscale updraft with a peak average strength of 46 cm s^{-1} was deduced from a dual Doppler analysis (Matejka and Ziegler 1990) and used as an input to a one-dimensional model. This model predicted presence of small graupel due to the coexistence of ice particles and significant amounts of supercooled cloud liquid. Radar observations of the reflectivity field within the stratiform region reveal small-scale reflectivity perturbations with amplitudes of about 10 dBZ (Fig. 1b). We speculate that these may have contained stronger updrafts in which riming growth of graupel could be further accelerated, in turn stimulating reflectivity growth. Indeed, variations of about 2 m s^{-1} were observed in the radial velocity measured at nadir with the Doppler radar on the P-3 aircraft. Although differential reflectivity data above the melting level is zero or slightly negative as is expected for small graupel (Aydin and Seliga 1984), this polarimetric signature is not sufficient to confirm the presence of graupel.

Our observations are similar to those reported by Willis and Heymsfield (1989) with four noticeable differences. First, the peak reflectivity factor on 3 June was 37 dBZ (Fig. 5a), whereas it was 27 dBZ in the dataset analyzed by Willis and Heymsfield (1989). Hence, the present case is characterized by relatively high precipitation and bulk melting rates. Second, neither the aircraft nor the radiosonde profiles (Fig. 2a) revealed an isothermal layer just below the melting level of the stratiform region on 3 June, whereas Willis and Heymsfield reported an isothermal layer in their case. Two competing mechanisms dictate the lapse rate in the melting layer. Heat exchange between melting hydrometeors and air tends to equalize the temperature;

opposed to this is the adiabatic warming promoted by downward motion of air. We speculate that this warming is dominant in our case. Third, these authors deduced maximum aggregates to be about 6 mm in diameter, while our cloud probe encountered some sizes of at least 11.25 mm and scientists on board the aircraft also witnessed large aggregates. Last, our observations and model calculation indicate the existence of graupel and rather high cloud liquid content (about 0.4 g kg^{-1}) above the melting layer, whereas the Willis and Heymsfield case apparently did not contain significant liquid cloud or graupel.

b. *Large hydrometeors in the melting layer*

The differential phase measurement through the melting layer and a scattering model lead us to speculate that hydrometeors larger than 6 mm were present. Measurements of differential phase indicate that there were aggregates just below the zero degree isotherm (3.4 km) in the size range of 7–10 mm. Further below (at about 3 km, temperature of 2°C), a characteristic transition in the sign of the differential phase shift upon scattering implies that some aggregates have grown to sizes of about 12 mm. According to Willis and Heymsfield, "the production of very large aggregates after the onset of melting can be accounted for by an increase in the terminal velocity difference between similar-sized hydrometeors, which results from differing degrees of melting and possibly from enhanced sticking due to partial melting." It is noteworthy that Humphries and Barge (1979) used a two-wavelength radar to deduce presence of 10–20-mm size wet aggregates at the bottom of the melting layer. Such large sizes are also inferred by Srivastava et al. (1986), who report terminal velocities of 9 m s^{-1} at about 1.2 km below the reflectivity peak in a stratiform region of an MCS; these velocities correspond to drops with diameters larger than 4 mm that must have originated from considerably larger aggregates. The terminal velocities (from Doppler data obtained with the antenna on the P-3 aircraft pointing at nadir) are found to be at most 7 m s^{-1} below the melting layer. These suggest drop sizes of about 2 mm in diameter. According to measurements by Fujiyoshi (1986), aggregate sizes from which these drops melted would have been between 10 and 15 mm. Observation of large aggregates was not reproduced by our cloud model because it does not attempt to parameterize the size and concentration changes due to enhanced sticking of snow particles in the melting layer.

c. *Backscattering in the bright band*

From the examination of the polarimetric measurands and the limited in situ observations, the following conceptual model of the processes that contribute to backscattering signatures in the bright band emerges. Wetting of ice hydrometeors results in a rapid increase in reflectivity and an increase of K_{DP}, both of which peak at the same height. From there on, two processes seem to dominate; some larger aggregates continue to grow and stabilize their orientation, while smaller ones collapse into raindrops. This growth is evident by the increase of differential phase shift upon scattering δ from small negative values at the location of peak reflectivity (200 m below the 0°C level) to about 4° at the location of the Z_{DR} maximum (900 m below the 0°C isotherm). The drop in correlation of horizontally and vertically polarized echoes between these two peaks is caused by the variations of δ.

A schematic in Fig. 9 illustrates the evolution of the hydrometeor distribution through the melting layer with height; we hypothesize that this evolution captures the dominant physical mechanism contributing to the observed polarimetric signatures. At the height of maximum reflectivity, most of the hydrometeors are wet but still preserve the crystal shape. Below this height, small hydrometeors collapse into drops, which is seen as the abrupt shift toward smaller sizes; the largest aggregates increase in size and concentration. Further below, only the largest aggregates survive and some increase, but all eventually break into drops.

7. Conclusions

Vertical profiles of polarimetric variables were obtained through the stratiform region of a mesoscale convective system. In addition, in situ measurements of precipitation types and model predictions were examined. Qualitative agreement between the three is found. A slight positive differential reflectivity at the top of the system is attributed to horizontally oriented plates and needles, both of which were observed by the airborne two-dimensional cloud probe. In midlevels

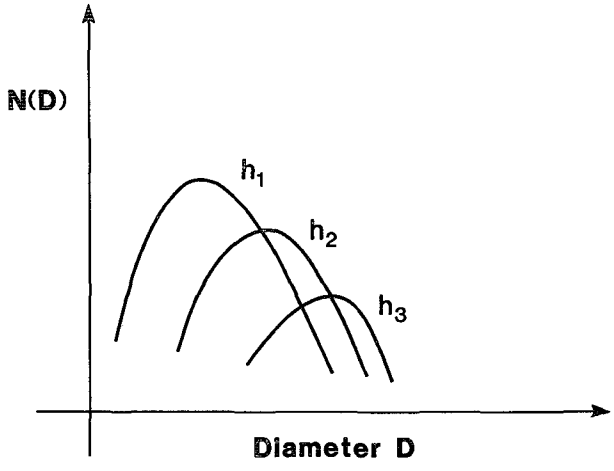

FIG. 9. Qualitative depiction of change with height of the distribution of hydrometeors in the melting layer. Heights decrease from h_1 to h_3.

(3.5–6 km), graupel is present in both observation and model; it could have caused slight negative differential reflectivities. According to the model, the observed mesoscale updraft (up to 46 cm s^{-1}) could have contributed to graupel formation by providing a source of supercooled cloud droplets for riming growth of ice particles. Variability in the reflectivity field was about 10 dBZ; this suggests that localized updrafts were present and may have enhanced the flux of supercooled water and thus formation of graupel. Frequency of graupel occurrence in the stratiform regions of mesoscale convective systems is not known; the model and physical reasoning suggest that it is a transient feature, which might also explain why it has not been observed more often. As the cloud glaciates, the source of graupel disappears, and thus we expect it to be absent in older MCSs. Observations of MCSs evolution with polarimetric radars could be used to verify this hypothesis.

Measurements indicate the presence of up to 0.4 g kg^{-1} of supercooled liquid water above the melting layer within the same height range as predicted by the model. This is a rather large value for an MCS. Another unusual feature of this MCS is that the stratiform region was detached from active convection. Although there is little data on the amount of supercooled liquid water in the stratiform part of MCSs, we argue that this may be very important for precipitation processes and polarimetric signatures there. The presence of supercooled liquid cloud may also play an important role in electrification.

There is a strong evidence that a dip in the $\rho_{hv}(0)$ at 400 m below the peak of reflectivity associated with the melting layer has been caused by the differential phase shift upon scattering from particles in the neighborhood of 10 mm in diameter; other contribution could have come from coexistence of frozen and liquid hydrometeors. It was found that aggregates continued to grow (>10 mm), and some survived 900 m below the 0°C isotherm; we attribute the increase in Z_{DR} to their elongated shape and stable orientation just before collapse into water drops. A conceptual model consistent with this data is proposed; it suggests a height-dependent distribution of aggregates with a modal value that increases and a concentration that decreases at lower heights.

The crucial polarimetric measurand in this research was the differential phase between the horizontally and vertically polarized echoes. It has provided us with a unique signature through the melting layer from which we are able to deduce the maximum sizes of hydrometeors. Propagation through oriented hydrometeors produces monotonically increasing differential phase shift. Appreciable deviation from the intrinsic differential propagation phase is attributed to the differential phase shift upon scattering δ. Scattering models predict the variation of δ with size, which can then be compared with measurements to infer the hydrometeor size and the electromagnetic bulk properties of the scatterers. None of these inferences could be made from the observations of the reflectivity factor alone.

Acknowledgments. During this study Dr. Balakrishnan was supported by the National Severe Storms Laboratory through a grant to the Cooperative Institute for Mesoscale Meteorological Studies. Participation in data collection for Dr. Aydin was supported by the Army Research Office under Contract DAAL 03-89-K-0158 and the National Science Foundation under ATM-8921014. Dr. Bringi was supported by the U.S. Army Research Office through the Center for Geosciences at Colorado State University. Mike Schmidt operated the radar during data collection and Yosepha Gal-Chen helped with various aspects of computer manipulations. Steve Hunter and Paul Willis gave us valuable advice concerning interpretation of cloud probe data, while Terry Shuur provided Fig. 1a. V. Chandrasekar contributed to the data collection effort. Part of this work has resulted from continuing support by the Joint System Program Office of the NEXRAD.

APPENDIX

A Modified Snow Parameterization

The earlier version of the cloud model (Ziegler 1985) has been modified to incorporate snow-particle aggregation. The total concentration and mixing ratio of snow particles are presently treated as independent variables, whereas in the earlier version only the mixing ratio was varied. This allows the model to approximate the aggregation process in which binary collision of snow particles followed by sticking or interlocking results in increased size and reduced total concentration without a corresponding change of the mixing ratio. Modeling aggregation is facilitated by the assumption of a gamma size distribution in place of the exponential function previously assumed for snow particles. This Appendix documents the new aggregation parameterization as well as further modifications of the snow parameterization necessitated by the choice of the gamma distribution for snow.

a. Terminal fall speed of snow

The parameterization employs a mass-weighted average terminal fall speed for snow particles. As the first step in deriving average fall speed, the following formula is adopted for the fall speed of a riming hexagonal crystal (Lin et al. 1983):

$$V_t = 153\left(\frac{\rho_0}{\rho}\right)^{1/2} D^{1/4}, \qquad \text{(A1)}$$

where the terminal fall speed V_t has units of centimeters per second, the equivalent spherical diameter D has units of centimeters, ρ is air density, and ρ_0 is a reference density of 10^{-3} g cm^{-3}. Converting from diameter to volume dependence, (A1) takes the form

$$V(v) = 153\left(\frac{6}{\pi}\right)^{1/12}\left(\frac{\rho_0}{\rho}\right)^{1/2} v^{1/12}. \quad \text{(A2)}$$

Note that a typical melted snow particle occupies only a fraction of this spherical volume [up to $O(10\%)$], in contrast to a liquid drop, which would fill the entire volume at a density of 1 g cm^{-3}. This is parameterized in the model by adopting a bulk snow-particle density $\rho_s = 0.1$ g cm^{-3}. (The snow particle mass is simply $m = \rho_s v$.)

The parameterization assumes that snow particles are distributed in the form of a gamma function of volume v. This is the same function as used for the cloud-droplet and raindrop distributions. The snow-particle distribution is written as

$$N(v) = N_s(\nu_s + 1)^{\nu_s+1} \times \left(\frac{v}{v_s}\right)^{\nu_s} \frac{\exp[-(\nu_s + 1)v/v_s]}{\Gamma(\nu_s + 1)v_s}, \quad \text{(A3)}$$

where N_s is the total concentration, v_s is the mean volume, and ν_s is the shape parameter. (The earlier model version assumed that the snow particles were distributed according to an exponential function.) Although the shape parameter may vary somewhat in gamma models of natural snow distributions, we assume a constant value of -0.8 for these model runs. This is the same value as the rain shape parameter, so that the meltwater drop size distributions and snow distributions at the melting level should have the same shapes in the model (as they do in observed stratiform regions). The resulting shape is broadly similar to that of an exponential function, a widely quoted model for snow size distributions. In the case where $\nu < 0$, the gamma distribution has a smaller slope than the exponential function in the range of intermediate particles sizes (around 1-mm diameter) and a steeper slope than the exponential function over a range of small and large particle sizes.

An expression for average fall speed may be obtained by evaluating the ratio of two integrals, where the upper integrand is the product of V_t, v, and $n(v)$, while the lower integrand is the product of v and $n(v)$. Evaluation of this integral ratio after substituting (A2) and (A3) yields an expression for the volume- (mass-) weighted snow-particle fall speed of the form

$$V_t(v_s) = \frac{153(6/\pi)^{1/2}\Gamma(\nu_s + 25/12)}{(\nu_s + 1)^{13/12}\Gamma(\nu_s + 1)}\left(\frac{\rho_0}{\rho}\right)^{1/2} v_s^{1/12}. \quad \text{(A4)}$$

b. Aggregation of snow

Although aggregation is analogous to raindrop self-collection, a number of complicating factors make it more difficult to model. For example, fall speeds of equally sized particles may vary as a complicated function of growth habit. Furthermore, empirical data on sticking–interlocking efficiency is lacking. (Conversely, collection kernel data for warm-rain coalescence is known with much better precision.) Following Passarelli (1978) and Heymsfield (1986), aggregation efficiencies that are independent of particle size and fall speeds approximated by single-valued functions of size are used to evaluate the collection kernel. Specifically, we adapted the existing parameterization of raindrop self-collection to the snow-particle aggregation process as follows.

The gravitational collection kernel (Long 1974) was computed separately for snow particles and raindrops over the radius range 0.01–0.5 cm in radius increments of 0.01 cm. The kernels were evaluated with the fall-speed formulas used by Passarelli (1978). The rain-collection kernels approximated by this technique compared satisfactorily with more precise values presented by Long (1974). The ratios of the gravitational collection kernels for equally sized snow particle and raindrop pairs were then computed. These ratios were approximately constant, ranging from 0.087 to 0.171 with a mean of 0.104. Assuming that snow particles and raindrops of a given spherical equivalent volume have collection kernels in a fixed ratio ϵ, the collection kernel for snow is approximated by the expression

$$K(v, u) = \epsilon E_a a_2 (v + u), \quad \text{(A5)}$$

where v and u are, respectively, the collector and collected particle volumes, E_a is the sticking–interlocking efficiency, and a_2 is the polynomial kernel coefficient (Long 1974). Substituting the snow distribution and the polynomial snow-collection kernel into the stochastic coalescence equation (SCE) and integrating over all volumes, we obtain an expression for the rate of change of snow-particle concentration by aggregation in the form

$$\frac{dN_s}{dt} = -a_2 \epsilon E_a N_s^2 v_s. \quad \text{(A6)}$$

This derivation is analogous to the SCE solution for rain self-collection reported in Ziegler (1985). (Note that the terms *coalescence* and *aggregation* are used interchangeably in applying the SCE to snow aggregation.) Following Lin et al. (1983), a simple exponential dependence of the aggregation efficiency on undercooling is assumed, specifically $E_a = \exp(0.05T)$, where T (°C) is temperature. This expresses an exponential increase of E_a from 0.1 at −45°C to 1.0 at the melting level. Aggregation does not change the mixing ratio of snow.

c. Snow deposition

The growth of snow particles by vapor deposition is analogous to cloud-droplet condensation growth, except that the effects of nonspherical geometry and ventilation due to fall velocity must be considered. More

specifically, the capacitance of a thin disk $C = 2r/\pi$ is formally substituted for radius r, while a ventilation factor is incorporated to account for the enhancement of local vapor gradients by particle fall speed. A kinetic equation of the form $\partial/\partial t[n_s(v)] = -\partial/\partial v[n(v)dv/dt]$ governs the evolution of the distribution accompanying the growth of individual droplets. The equation governing individual ice crystal growth by diffusion (e.g., Pruppacher and Klett 1978) was substituted along with the size distribution function for snow particles into the kinetic equation. After integrating over all particle volumes and rearranging terms, the resulting expression for the rate of change of snow mixing ratio from deposition is

$$\frac{dq_s}{dt} = 4\left(\frac{6}{\pi}\right)^{1/3} \frac{\Gamma(\nu_s + 4/3)v_s^{1/3}F_dF_vN_s}{\rho\rho_s(\nu_s + 1)^{1/3}\Gamma(\nu_s + 1)}, \quad \text{(A7)}$$

where $F_v = 0.65 + 0.44N_{Sc}^{1/3}N_{Re}^{1/2}$ is the ventilation factor for snow (Thorpe and Mason 1966), $F_d = s_i - [L_s^2/(K_aR_vT^2) + R_vT/(D_ve_{si})]^{-1}$, and $s_i = q_v/q_{si}$ is the saturation ratio with respect to ice. In these expressions, q_{si} and e_{si} are, respectively, the saturation mixing ratio and the vapor pressure with respect to ice, L_s is the latent heat of sublimation, K_a is the thermal conductivity of air, R_v is the gas constant for water vapor, D_v is the vapor diffusivity, and T is absolute temperature. The Schmidt number N_{Sc} takes the value 0.6. The Reynolds number N_{Re} is approximated as a distribution average by the expression $N_{Re} = V_tD_s\rho/\mu$, where the average snow-particle fall speed V_t is specified by (A2), the mean diameter $D_s = (3v_s/4\pi)^{1/3}$, and the dynamic viscosity μ takes a value of 1.7×10^{-4} g cm^{-1} s^{-1}. The Schmidt number and dynamic viscosity take values appropriate to conditions at the melting level. Deposition does not change the total concentration of snow.

d. Collection of cloud water by snow

The collection of cloud droplets by snow is analogous to rain collection of cloud droplets, although collision efficiency must be modified for the effect of the low bulk density of snow particles. Because air can flow between the branches of a snow particle, the collision efficiency is less than unity. (The sticking efficiency is assumed to be unity.) The rate of mass accumulation is proportional to the accretion efficiency E_{sc}, the product of the collision, and the sticking efficiencies. In these runs, $E_{sc} = 0.5$ is assumed. Substituting snow distribution parameters into (A12) in Ziegler (1985), the resulting expression for the rate of change of snow mixing ratio from cloud-droplet collection is

$$\frac{dq_s}{dt} = a_2\epsilon E_{sc}N_cN_sv_c\rho_s \frac{[(\nu_c + 2)v_c/(\nu_c + 1) + v_s]}{\rho}. \quad \text{(A8)}$$

Collection of cloud water does not change the total concentration of snow. The mixing ratio of cloud droplets is, however, decreased according to conservation of total mass, while the total concentration of cloud droplets is adjusted according to the moment relation $N_cv_c = \rho q_c$, assuming that the droplet mean volume v_c is constant during the process (Ziegler 1985).

e. Collection of cloud ice by snow

The collection of cloud ice by snow is analogous to collection of cloud water droplets by snow. Cloud ice particles are assumed to be distributed according to a gamma function of volume like those for the cloud, rain, and snow distributions (Ziegler 1985; Ziegler et al. 1986). We assume, however, that the mean volume v_i is constant and predict the mixing ratio only. This permits diagnosis of cloud ice concentration N_i according to the moment relation $\rho_iN_iv_i = \rho q_i$, where $\rho_i = 0.9$ g cm^{-3} and $v_i = 5.23 \times 10^{-10}$ cm^3. Substituting cloud ice distribution parameters into (A8), the resulting expression for the rate of change of snow mixing ratio from cloud ice collection is

$$\frac{dq_s}{dt} = a_2\epsilon E_{si}N_iN_sv_i\rho_s \frac{[(\nu_i + 2)v_i/(\nu_i + 1) + v_s]}{\rho}. \quad \text{(A9)}$$

In these runs $\nu_i = 0$ and $E_{si} = 0.1$ are assumed. Collection of cloud ice does not change the total concentration of snow. The mixing ratio of cloud ice is, however, decreased according to conservation of total mass, while the total concentration of cloud ice is decreased assuming that the droplet mean volume v_i is constant during the process (Ziegler 1985). Snow concentration is not affected by collection of cloud ice.

f. Snow melting

The parameterization of snow melting is based on an expression for the melting rate of an individual snow particle of the form (Wisner et al. 1972)

$$\frac{L_f\pi\rho_sD^2}{2}\frac{dq_s}{dt} = -2\pi F_vF_mD, \quad \text{(A10)}$$

where $F_m = K_a(T - T_0) + L_vD_v\rho(q_v - q_{vs})$, q_v is vapor mixing ratio, q_{vs} is the saturation mixing ratio with respect to water, and other terms are as previously defined. The governing kinetic equation takes the same form as the equation governing deposition growth, except that the expression for individual particle decay is used. After converting (A10) from size to volume dependence, substituting the size distribution into the kinetic equation, and integrating over all volumes, the resulting expression for the rate of change of snow mixing ratio from melting is

$$\frac{dq_s}{dt} = -\frac{3.6\pi^{2/3}F_v F_m}{L_f \rho \rho_s \Gamma(\nu_s + 1)} (\nu_s + 1)^{-1/3} \times \Gamma(\nu_s + 4/3) v_s^{1/3} N_s. \quad \text{(A11)}$$

The snow concentration is adjusted from the moment relation $\rho_s N_s v_s = \rho q_s$ under the assumption that v_s is a constant. Since crystal collapse and water accumulation increase the bulk particle density, the melting calculation uses $\rho_s = 0.5$ g cm^{-3} ($T > 273.16$ K).

g. *Radar reflectivity of snow*

The expression for the radar reflectivity of the snow distribution is formally identical to the corresponding expression for rain reflectivity (Ziegler 1985). This expression, however, must be adjusted for the ratio of the dielectric constants of ice and water and the low bulk density of the snow particles. The resulting equation takes the form

$$Z = 3.6 \times 10^{12} \frac{|K_i|^2}{|K_r|^2} \frac{(\nu_s + 2)}{(\nu_s + 1)} N_s v_s^2, \quad \text{(A12)}$$

where the correction for low snow-particle density includes the ice dielectric constant $|K_i|^2 = 0.243\rho_s^2$ and the rain dielectric constant $|K_r|^2 = 0.93$. The effect of wetting during melting is not considered.

REFERENCES

Aydin, K., and T. A. Seliga, 1984: Radar polarimetric backscattering properties of conical graupel. *J. Atmos. Sci.*, **41**, 1887–1892.

Balakrishnan, N., and D. S. Zrnić, 1990a: Estimation of rain and hail rates in mixed-phase precipitation. *J. Atmos. Sci.*, **47**, 565–583.

——, and ——, 1990b: Use of polarization to characterize precipitation and discriminate large hail. *J. Atmos. Sci.*, **47**, 1525–1540.

Battan, L. J., 1973: *Radar Observation of the Atmosphere.* University of Chicago Press.

Doviak, R. J., and D. S. Zrnić, 1984: *Doppler Radar and Weather Observations.* Academic Press, 458 pp.

Fujiyoshi, Y., 1986: Melting snowflakes. *J. Atmos. Sci.*, **43**, 307–311.

Heymsfield, A. J., 1986: Ice particle evolution in the anvil region of a severe thunderstorm during CCOPE. *J. Atmos. Sci.*, **43**, 2463–2478.

Humphries, R. G., and B. L. Barge, 1979: Polarization and dual-wavelength radar observations of the bright band. *IEEE Trans. Geos. Elect.*, **GE-17**, 4, 190–195.

Illingworth, A. J., and I. J. Caylor, 1989: Cross polar observations of the brightband. Preprints, *24th Conf. on Radar Meteorology,* Tallahassee, Amer. Meteor. Soc., 323–327.

Jameson, A. R., 1989: The interpretation of meteorological application of radar backscatter amplitude ratios at linear polarizations. *J. Atmos. Oceanic Technol.*, **6**, 908–919.

Knollenberg, R. G., 1970: The optical array: An alternative to scattering or extinction for airborne particle size determination. *J. Appl. Meteor.*, **9**, 86–103.

Lin, Y.-L., R. D. Farley, and H. D. Orville, 1983: Bulk parameterization of the snow field in a cloud model. *J. Climate Appl. Meteor.*, **22**, 1065–1092.

Long, A. B., 1974: Solutions to the droplet collection equation for polynomial kernels. *J. Atmos. Sci.*, **31**, 1040–1052.

Matejka, T., and C. Ziegler, 1990: The effect of hydrometeor evolution on dynamical processes in the stratiform region of a mesoscale convective system. Preprints, *Conf. on Cloud Physics,* Amer. Meteor. Soc., Boston, 678–682.

Meischner, P. F., V. N. Bringi, D. Heimann, and H. Holler, 1991: A squall line in Southern Germany: Kinematic and precipitation formation as deduced by advanced polarimetric Doppler radar measurements. *Mon. Wea. Rev.*, **119**, 678–701.

Moninger, W. R., V. N. Bringi, T. R. Detman, J. R. Jordan, T. A. Seliga, and K. Aydin, 1984: Melting layer observations during MAYPOLE. Preprints, *22nd Radar Meteorology Conference,* Zurich, Amer. Meteor. Soc., 364–369.

Passarelli, R. E., Jr., 1978: An approximate analytic model of the vapor deposition and aggregation growth of snowflakes. *J. Atmos. Sci.*, **35**, 118–124.

Pruppacher, H. R., and J. D. Klett, 1978: *Microphysics of Clouds and Precipitation.* Reidel, 714 pp.

Rutledge, S. A., and P. V. Hobbs, 1983: The mesoscale and microscale organization of clouds and precipitation in midlatitude cyclones. VIII: A model for the seeder–feeder process in warm-frontal rainbands. *J. Atmos. Sci.*, **40**, 1185–1206.

Srivastava, R. C., T. J. Matejka, and T. J. Lorello, 1986: Doppler radar study of the trailing anvil region associated with a squall line. *J. Atmos. Sci.*, **43**, 356–377.

Thorpe, A. D., and B. J. Mason, 1966: The evaporation of ice spheres and ice crystals. *Brit. J. Appl. Phys.*, **17**, 541–551.

Waterman, P. C., 1969: Scattering by dielectric obstacles. *Alta Freq.*, **38**, 348–352.

Willis, T. W., and A. J. Heymsfield, 1989: Structure of the melting layer in mesoscale convective system stratiform precipitation. *J. Atmos. Sci.*, **46**, 2008–2025.

Ziegler, C. L., 1985: Retrieval of thermal and microphysical variables in observed convective storms. Part I: Model development and preliminary testing. *J. Atmos. Sci.*, **42**, 1487–1509.

——, P. S. Ray, and D. R. MacGorman, 1986: Relations of kinematics, microphysics, and electrification in an isolated mountain thunderstorm. *J. Atmos. Sci.*, **43**, 2098–2114.